DEFORMATION-AWARE SIMULATOR FOR HANDHELD ULTRASOUND IMAGING

Ziyi Chen[1], *Shaifali Parashar*[2], *and Adrian Basarab*[1]

[1]CREATIS, Universite Claude Bernard Lyon 1, INSA-Lyon, CNRS, INSERM, UMR5220, U1294, France
[2]LIRIS, CNRS, Ecole Centrale de Lyon, INSA Lyon, University Claude Bernard Lyon 1, UMR5205, France

ABSTRACT

Realistic ultrasound simulation is essential for training and algorithm development. However, most existing methods generate single-frame images from thin slices of the probe's field of view, neglecting tissue deformation and spatial continuity across frames. We propose a physics-based simulation pipeline, fully compatible with any scatterer-based ultrasound simulator, which employs finite element modeling to update local scatterer maps under large-scale stability constraints, given the probe trajectory and tissue geometry. The framework produces continuous and anatomically accurate ultrasound sequences with physically consistent speckle evolution, providing a practical tool for training, visualization, and the development of freehand ultrasound reconstruction algorithms.

Index Terms— Freehand ultrasound imaging, simulation, tissue deformation

1. INTRODUCTION

Ultrasound (US) is a real-time, safe, and cost-effective medical imaging modality. A distinctive feature of US imaging is the speckle pattern, caused by echoes scattered by numerous disordered microscopic structures, usually referred to as scatterers. Unlike electronic noise, speckle exhibits pronounced temporal and spatial coherence.

US simulation refers to generating synthetic images and serves as a powerful tool not only for operator training, but also for evaluating image processing methods and providing datasets for training deep learning algorithms. The most popular methods consider the medium as a dense distribution of point scatterers, each with assigned random intensity and spatial position. Depending on how US wave propagation is modeled, three categories of approaches can be distinguished. Wave-based methods, such as Field II [1] and SIMUS [2], directly solve acoustic equations and achieve high physical fidelity, though at considerable computational cost. Convolution-based methods approximate imaging as a convolution of the scatterer map with the system's point spread function (PSF) [3], enabling efficient speckle synthesis for real-time use. Ray-tracing approaches model geometric effects such as reflection, refraction, and attenuation, producing images with strong visual realism [4, 5], hence less in phase with the physics of ultrasound. Less popular, methods that do not explicitly model scatterers rely on deep generative models to synthesize ultrasound images or videos [6, 7, 8], often prioritizing visual style similarity while overlooking the physical consistency of speckle patterns.

Most existing US simulators focus on generating in-plane 2D temporal image sequences, thus accounting only for temporal speckle coherence, while neglecting the spatial coherence across consecutive slices that arises in freehand probe scanning. In practice, speckle patterns evolve smoothly along a scanning trajectory, and preserving this continuity in simulations is crucial for validating various algorithms such as speckle tracking or 3D reconstruction [9]. Simulating such large-scale spatial coherence requires maintaining a consistent scatterer map with sufficient scatterer density (i.e., tens of scatterers per resolution cell to ensure fully-developped speckle) across the probe's scanning range, which leads to prohibitive memory demands [10].

We recently proposed a spatially coherent US simulator (SCUS) [10], based on scatterer distributions within 3D cells across the entire simulated medium, while applying random perturbations to each block. This strategy preserves the randomness and statistical properties of speckle, while substantially reducing memory consumption, thereby enabling the simulation of large-scale spatial coherence in ultrasound imaging. Nevertheless, SCUS relies on a tissue rigid-body assumption and therefore neglects the elastic nature of probe–tissue interactions [11]. In practice, probe pressure compresses the medium and induces deformation, which manifests in US images as apparent displacements of anatomical structures. Realistic modeling of this phenomenon requires the incorporation of biomechanical representations of tissue elasticity.

Herein, we achieve realistic ultrasound image simulation from freehand probe trajectories recorded with a position tracker, reproducing probe-induced anatomical deformations while preserving spatial coherence between adjacent slices. The finite element method (FEM) is employed to model tissue elasticity and guide the deformation of the scatterer map. Furthermore, we propose a complete pipeline that mimics the acquisition of 2D ultrasound image sequences in current handheld clinical practice.

2. PROPOSED METHODOLOGY

We propose a four-stage pipeline that integrates three key components: back-projection of probe positions, field-of-view (FoV) expansion, and deformation-driven scatterer update, as illustrated in Fig. 1. Given the initial tissue configuration and a time-varying probe trajectory, the scatterer distribution across the medium remains fixed to ensure speckle spatial coherence. For each frame, the deformation field is computed from the probe motion and applied to update the positions of scatterers within the current FoV, which are then used for ultrasound image synthesis.

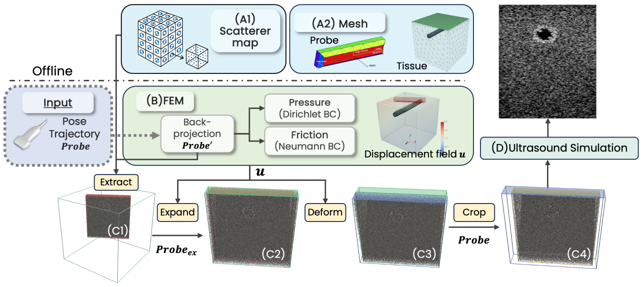

Fig. 1. **Overall workflow of the proposed pipeline.** Stage A performs offline preprocessing, and an ultrasound sequence is generated by repeating Stages B–D. The bottom row shows scatterer map changes during Stage C: red, green, blue, and yellow denote the initial FoV, expanded FoV, deformed region, and final map for image synthesis.

2.1. Geometry and scatterer initialization

The anatomical geometry of the simulated medium and the acoustic and mechanical properties of each tissue are first defined. The geometry may be either a simplified model as considered in this work, or a realistic one derived for example from 3D imaging modalities such as CT or MRI.

Scatterer generation. Scatterers are points in the 3D space that enable the diffusion of the ultrasound waves, similar to smaller than wavelength structures in real tissues. They are defined by their 3D position and amplitude, both following random distributions. Herein, the efficient pseudo-random strategy proposed in SCUS [10] is used to generate the positions. Each scatterer's amplitude is sampled from a scaled normal distribution according to the echogenicity of the corresponding tissue type.

Mesh generation. In parallel, tetrahedral meshes are generated for FEM simulations based on the defined geometry, consisting in N nodes. The probe is represented as a rounded rectangular cuboid whose contact surface corresponds to the transducer's aperture dimensions (width and height). A fillet radius of 2 mm is applied to approximate the curved shape of the transducer face. The upper surface of the medium is locally refined to ensure precise contact pair with the probe and accurate contact-force computation.

2.2. FEM-based deformation modeling

Tissue deformation induced by probe–tissue contact is formulated as a quasi-static rigid–elastic sliding contact problem with friction, modeled using the open-source finite element framework *FEniCSx* [12].

Mechanical assumptions. At time t, the ultrasound probe $Probe(P_t, R_t, FoV)$ is characterized by its surface-center position $P_t \in \mathbb{R}^3$, rotation matrix $R_t \in \mathbb{R}^{3\times3}$, and field-of-view dimensions $FoV \in \mathbb{R}^3$. It is modeled as a rigid body that exerts normal pressure and tangential frictional forces on the contact surface with the medium, thereby inducing its deformation. The medium is assumed to behave as a linear elastic material under small deformations, governed by (the body force is assumed equal to 0):

$$\nabla \cdot \boldsymbol{\sigma_t} = 0, \quad \boldsymbol{\sigma_t} = \mathbf{C}\boldsymbol{\varepsilon_t}, \quad \boldsymbol{\varepsilon_t} = \tfrac{1}{2}(\nabla \boldsymbol{u_t} + \nabla \boldsymbol{u_t}^{\mathsf{T}}), \quad (1)$$

where $\boldsymbol{\sigma_t} \in \mathbb{R}^{N\times3}$ is the Cauchy stress tensor, $\boldsymbol{u_t} \in \mathbb{R}^{N\times3}$ the 3D displacement field at probe trajectory time t, $\mathbf{C}$ the elasticity tensor defined by each tissue's Young's modulus and Poisson's ratio, and $\boldsymbol{\varepsilon}$ the strain. The bottom surface of the tissue is fixed, while the lateral boundaries are traction-free. The contact interaction between the probe and the tissue is governed by the boundary conditions described below, with contact possibly occurring along the rounded probe edges depending on the probe inclination.

Back-projection of probe positions. For each probe pose defined by position and orientation (P_t, R_t), the corresponding contact pose on the undeformed tissue boundary is obtained by back-projecting the probe position along its surface normal until intersection with the undeformed medium. This yields the reference pose(P'_t, R_t), representing the initial contact configuration prior to deformation, which serves as the geometric basis for defining displacement boundary conditions.

Implicit pressure term: rigid probe displacement (Dirichlet boundary condition). To avoid the need of force information, difficult to have in practical situations, we propose to determine the contact pressure implicitly by the Dirichlet boundary condition applied to the prescribed probe trajectory. The probe displacement field is expressed as

$$\boldsymbol{u}_t(\boldsymbol{x}) = (P_t - P'_t) + R_t(\boldsymbol{x} - P'_t), \quad (2)$$

where $\boldsymbol{x}$ is any node on the probe surface. This displacement is imposed as the boundary condition on the probe and transferred to the tissue nodes in contact using the reaction force formulation.

Friction term: adhesion friction (Neumann boundary condition). In addition to the normal traction, adhesion-type friction at the medium–probe interface is considered, while the deformation-related friction component is neglected [13]. Following the model proposed by Adams et al. [14], the interfacial shear stress τ increases linearly with the local pressure:

$$\tau = \tau_0 + \alpha p, \quad (3)$$

where τ_0 is the intrinsic interfacial shear strength, α is a pressure coefficient, and p is the local normal pressure transmitted through the contact. This pressure-dependent adhesion model is used to mimic the frictional behavior of hydrated or wet skin under sliding contact.

2.3. Scatterer Deformation

Scatterer extraction. Instead of explicitly storing all scatterers, we adopt a cell-based data structure, following our previous work [10], which substantially reduces memory consumption. For a given probe pose $Probe(P_t', R_t, FoV)$, candidate cells intersecting the field of view are efficiently identified via spatial hashing, and the corresponding scatterers are retrieved from the predefined tissue-mimicking map to assemble a local scatterer map, as shown by the red box in Fig. 1(C1) [10].

Field-of-view expansion and deformation update. Probe compression redistributes scatterers, leading to misalignment between the extracted slice and the true deformed configuration. To address this, the probe's field of view is temporarily expanded to FoV_{ex} according to the maximum nodal displacement, as indicated by the green box in Fig. 1(C2). The displacement field obtained from FEM is then applied to update scatterer positions within the expanded region, producing the deformed distribution shown by the blue box in Fig. 1(C3). Finally, the updated scatterers are cropped back to the probe's actual field of view, forming the final yellow box in Fig. 1(C4), which is used for ultrasound image synthesis.

2.4. Ultrasound image simulation

The deformed scatterer map corresponding to the probe pose $Probe(P_t, R_t, FoV)$ is used for ultrasound image simulation with SIMUS [2], together with parameters defining the probe and the acquisition scheme.

3. RESULTS

To evaluate the effectiveness of the proposed framework, experiments were performed on a simplified vascular phantom model. The blood vessel is treated as a static structure, and blood flow velocity is not considered in the simulation. The vessel is represented by a hollow cylinder with an outer diameter of 6 mm, an inner diameter of 4 mm, and a wall thickness of 1 mm. The surrounding tissue is modeled as a cube with a side length of 60 mm. The probe simulated was a standard L11-5v transducer from Verasonics, with an aperture width of 38.4 mm, a height of 5 mm, and an imaging depth of 40 mm.

Twenty-one plane waves steered from –10° to 10° were compounded to form the simulated US image, which was log-compressed after envelope detection with a 40 dB dynamic range. The simulated images were cropped to a field of view of $(-15, 15)$ mm laterally and $(0, 20)$ mm axially in the probe coordinate system.

3.1. Speckle statistical validation

To validate the statistical consistency of speckle patterns generated by the proposed pipeline, we performed two complementary analyses at both the image and scatterer-map levels.

(1) B-mode speckle statistics. We first verified that the log-compressed envelope images produced by the proposed method exhibit log-Rayleigh distributed speckle, consistent with the statistical characteristics of fully developed speckle in real B-mode US. Simulations were conducted with the probe positioned at $P_t \in \{30, 57, 30\}$ mm and rotated by $\{0°, 10°, 0°\}$, under scatterer densities of 5, 15, 20, 25, and 40 scatterers per mm^3. The envelope signals were analyzed using the Kullback–Leibler (KL) divergence to quantify their deviation from the Rayleigh model, as summarized in Table 1. Results show that increasing scatterer density yields finer, more Rayleigh-like speckle patterns but at higher computational cost. A density of 20 scatterers per mm^3 (KL $\approx$ 0.1) achieves a favorable balance between realism and efficiency.

Table 1. B-mode image–level evaluation of SIMUS quality under different scatterer densities.

Density(mm^{-3})	5	15	**20**	25	40
KL div.	0.65	0.17	**0.10**	0.064	0.016
Time (s)	124	257	346	462	783
Scatterers	3.2k	9.7k	12.9k	16.1k	25.8k

(2) Scatterer-map uniformity. To further evaluate the statistical stability of the proposed framework, we compared it against two alternative scatterer-map configurations: (i) scatterers generated directly from probe-recorded positions P_t using [10], and (ii) deformation performed with the proposed method without the FoV expansion step. Spatial uniformity was quantified using the l_2-discrepancy metric, where lower values indicate higher uniformity in scatterer distribution.

Table 2. Discrepancy of scatterer maps generated by different methods ($\times 10^{-4}$).

Method	**5**	**15**	**20**	**25**	**40**
SCUS	7.60	5.18	4.43	4.68	2.72
Ours (w/o expand)	253.9	257.1	256.4	193.5	254.2
Ours	9.48	9.79	7.93	5.83	6.18

As shown in Table 2, the proposed method achieves a consistently low discrepancy, comparable to the initial configuration, indicating that the scatterer update module effectively preserves statistical uniformity during deformation. In contrast, omitting the FoV expansion step results in a two-order-of-magnitude increase in discrepancy due to directional scatterer drift, leading to void regions within the FoV. Overall, these results confirm that the proposed method maintains statistical consistency of the speckle field throughout deformation and highlight the critical role of the FoV expansion in ensuring spatial uniformity.

3.2. Deformation Validation

To evaluate the proposed method under realistic scanning conditions, the probe was tilted by 30° around the Y-axis and advanced along its normal direction with progressive $1\ \mathrm{mm}$ indentation across five frames. Small random perturbations (±3% in position, ±2° in orientation) were added to emulate hand-induced variability during freehand scanning. Demonstration videos are available at: https://github.com/ZyyyChen/DeformUS-Simulator.git

Figure 2 illustrates the US results during the probe motion. The first row shows the 3D model. The second row displays US images directly generated by SCUS. The third row shows images simulated only using the probe pose backprojection module (without tissue compression). The fourth row presents the images corrected by our proposed method. The SCUS-generated images exhibit severe probe penetration artifacts, particularly at larger indentation depths, and the vessel remains undeformed. Comparison shows that neglecting tissue compression leads to inaccurate vessel positioning, while the proposed method accurately captures the vessel flattening and upward shift caused by surrounding tissue compression, reflecting realistic tissue–probe interactions.

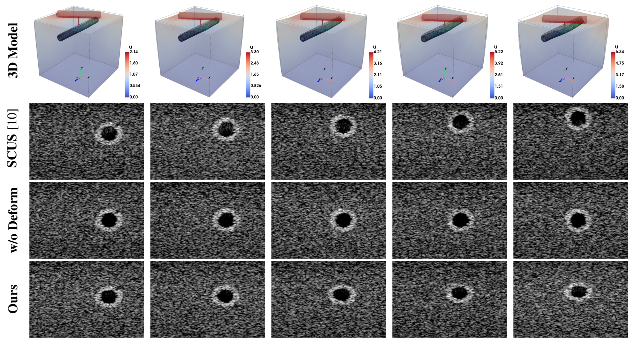

Fig. 2. Ultrasound simulation with progressive 1 mm forward and 1 mm indentation motion of the probe, incorporating 3% random perturbations to emulate realistic freehand variations. The proposed method accurately reproduces vessel deformation and upward displacement resulting from tissue compression.

3.3. Spatial consistency

To evaluate the spatial consistency of speckle patterns between adjacent frames, we analyzed the correlation of US images simulated during probe translation along the central axis, while maintaining a constant indentation depth of $3\ \mathrm{mm}$. As shown in Fig. 3, speckle patterns generated from independently reinitialized scatterers exhibit no spatial correlation across slices. In contrast, the proposed method preserves speckle consistency within approximately $0.2\ \mathrm{mm}$ of interslice distance, demonstrating its ability to maintain coherent speckle evolution during continuous probe motion.

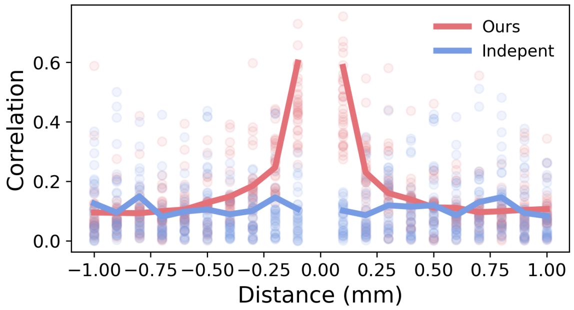

Fig. 3. Spatial correlation of speckle patterns versus interslice distance.

3.4. Friction analysis

In real ultrasound acquisitions, vessels often exhibit not only compression but also lateral displacement away from the probe due to pressure, especially in longitudinal scans with an oblique probe angle. This behavior, primarily caused by probe–skin adhesion friction [13], was successfully reproduced in our simulations. As shown in Fig. 4, the presence of friction induces noticeable lateral vessel motion, whereas in the frictionless case the vessel undergoes only compression without sideward displacement. These results highlight the essential role of friction in realistic probe–tissue interaction.

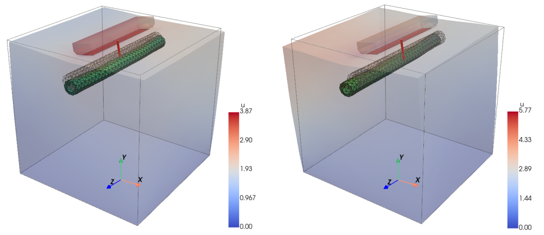

(a) Without friction (d) With friction

Fig. 4. Simulated vessel deformation without or with adhesion friction during probe compression.

4. CONCLUSION

We presented a physics-based scatterer deformation model and ultrasound simulation pipeline that generate continuous ultrasound sequences, reproducing realistic speckle evolution across frames and probe-induced anatomical deformation during handheld scanning, unlike conventional single-frame simulators. Building on an efficient scatterer extraction strategy, the proposed method models tissue compression, lateral displacement, and deformation caused by probe pressure and friction using only the recorded probe trajectory. Fully compatible with existing scatterer-based simulators and medium models, the framework provides valuable data for tasks requiring spatially coherent speckle patterns and anatomically accurate representations, such as 3D reconstruction and education.

5. COMPLIANCE WITH ETHICAL STANDARDS

This work uses only synthetic data.

6. ACKNOWLEDGMENTS

This work was supported by the LABEX PRIMES (ANR-11-LABX-0063) of Université de Lyon, within the program "Investissements d'Avenir" (ANR-11-IDEX-0007) operated by the French National Research Agency (ANR), and by Fédération Informatique de Lyon. The authors would also like to acknowledge the financial support of the China Scholarship Council (CSC).

7. REFERENCES

[1] Jørgen Arendt Jensen, "Field: A program for simulating ultrasound systems," *Medical & Biological Engineering & Computing*, vol. 34, no. sup. 1, pp. 351–353, 1997.

[2] Damien Garcia, "Simus: An open-source simulator for medical ultrasound imaging. part i: Theory & examples," *Computer Methods and Programs in Biomedicine*, vol. 218, pp. 106726, 2022.

[3] Hang Gao, Hon Fai Choi, Piet Claus, Steven Boonen, Siegfried Jaecques, G Harry Van Lenthe, Georges Van der Perre, Walter Lauriks, and Jan D'hooge, "A fast convolution-based methodology to simulate 2-dd/3-d cardiac ultrasound images," *IEEE transactions on ultrasonics, ferroelectrics, and frequency control*, vol. 56, no. 2, pp. 404–409, 2009.

[4] Benny Burger, Sascha Bettinghausen, Matthias Radle, and Jürgen Hesser, "Real-time gpu-based ultrasound simulation using deformable mesh models," *IEEE transactions on medical imaging*, vol. 32, no. 3, pp. 609–618, 2012.

[5] Rastislav Starkov, Lin Zhang, Michael Bajka, Christine Tanner, and Orcun Goksel, "Ultrasound simulation with deformable and patient-specific scatterer maps," *International journal of computer assisted radiology and surgery*, vol. 14, no. 9, pp. 1589–1599, 2019.

[6] Jiamin Liang, Xin Yang, Yuhao Huang, Haoming Li, Shuangchi He, Xindi Hu, Zejian Chen, Wufeng Xue, Jun Cheng, and Dong Ni, "Sketch guided and progressive growing gan for realistic and editable ultrasound image synthesis," *Medical image analysis*, vol. 79, pp. 102461, 2022.

[7] Benoit Freiche, Anthony El-Khoury, Ali Nasiri-Sarvi, Mahdi S Hosseini, Damien Garcia, Adrian Basarab, Mathieu Boily, and Hassan Rivaz, "Ultrasound image generation using latent diffusion models," in *Medical Imaging 2025: Ultrasonic Imaging and Tomography*. SPIE, 2025, vol. 13412, pp. 287–292.

[8] Tingxiu Chen, Yilei Shi, Zixuan Zheng, Bingcong Yan, Jingliang Hu, Xiao Xiang Zhu, and Lichao Mou, "Ultrasound image-to-video synthesis via latent dynamic diffusion models," in *International Conference on Medical Image Computing and Computer-Assisted Intervention*. Springer, 2024, pp. 764–774.

[9] Hengtao Guo, Hanqing Chao, Sheng Xu, Bradford J Wood, Jing Wang, and Pingkun Yan, "Ultrasound volume reconstruction from freehand scans without tracking," *IEEE Transactions on Biomedical Engineering*, vol. 70, no. 3, pp. 970–979, 2022.

[10] François Gaits, Nicolas Mellado, Gauthier Bouyjou, Damien Garcia, and Adrian Basarab, "Efficient stratified 3-d scatterer sampling for freehand ultrasound simulation," *IEEE Transactions on Ultrasonics, Ferroelectrics, and Frequency Control*, vol. 71, no. 1, pp. 127–140, 2023.

[11] Zhongliang Jiang, Yue Zhou, Yuan Bi, Mingchuan Zhou, Thomas Wendler, and Nassir Navab, "Deformation-aware robotic 3d ultrasound," *IEEE Robotics and Automation Letters*, vol. 6, no. 4, pp. 7675–7682, 2021.

[12] Igor A Baratta, Joseph P Dean, Jørgen S Dokken, Michal Habera, Jack HALE, Chris N Richardson, Marie E Rognes, Matthew W Scroggs, Nathan Sime, and Garth N Wells, "Dolfinx: the next generation fenics problem solving environment," 2023.

[13] M Kwiatkowska, SE Franklin, CP Hendriks, and K Kwiatkowski, "Friction and deformation behaviour of human skin," *Wear*, vol. 267, no. 5-8, pp. 1264–1273, 2009.

[14] Michael J Adams, Brian J Briscoe, and Simon A Johnson, "Friction and lubrication of human skin," *Tribology letters*, vol. 26, no. 3, pp. 239–253, 2007.